Journal of The
Electrochemical Society

Cold Co-Sintering Studies of Composite Cathode for All Solid-State Li Batteries

To cite this article: Khushnuda Nur *et al* 2025 *J. Electrochem. Soc.* **172** 013503

Journal of The Electrochemical Society, 2025 **172** 013503

Cold Co-Sintering Studies of Composite Cathode for All Solid-State Li Batteries

Khushnuda Nur,[1,2,3,z] Christoph Roitzheim,[1] Sandra Lobe,[1] Qianli Ma,[1] Martin Finsterbusch,[1,4] Martin Bram,[1,5] and Olivier Guillon[1,3,4]

[1]*Institute of Energy Materials and Devices: Materials Synthesis and Processing (IMD-2) Forschungszentrum Jülich GmbH, 52425 Jülich, Germany*
[2]*Department of Metallurgical and Materials Engineering, University of Engineering and Technology (UET) Lahore, Lahore 54890, Pakistan*
[3]*Rheinisch-Westfalische Technische Hochschule (RWTH) Aachen University, Institute of Mineral Engineering, 52064 Aachen, Germany*
[4]*Jülich Aachen Research Alliance, JARA-Energy, 52425 Jülich, Germany*
[5]*Ruhr-Universität Bochum, Institut für Werkstoffe, Universitätsstraße 150, 44801 Bochum, Germany*

In the present work, we applied cold sintering for the processing of $Li_{1.3}Al_{0.3}Ti_{1.7}(PO_4)_3$ (LATP) and then $LiMn_2O_4$/LATP/Carbon black composite cathode. Their high-temperature processing is challenging due to Li evaporation and undesirable diffusion between electrode and electrolyte, leading to high interfacial resistance between these components. Cold sintering can be an option to address these problems. For cold sintered LATP, X-ray diffraction analysis displayed only a minor amount of secondary phases, X-ray photoelectron spectroscopy showed slight reduction of Ti^{+4} to Ti^{+3} and Arrhenius plot presented higher activation energy for Li^+ conduction. Transferring this knowledge to our composite cathode, we got ∼85% relative density at merely 400 °C, 400 MPa using 1 molar aqueous solution of LiOH in a 1 min dwell time. To the best of our knowledge this is the first time a cold co-sintered composite cathode of this type has been prepared. It was wetted with polymer electrolyte and characterized electrochemically against a Li-metal anode. While the cell could be reversible cycled several times, proving the concept, impurity phases after cold sintering limited the extractable capacity. This detailed investigation contributes a deep insight of cold co-sintering application for composite cathodes.

 [DOI: 10.1149/1945-7111/ada82b]

Manuscript submitted October 21, 2024; revised manuscript received December 12, 2024. Published January 20, 2025.

Supplementary material for this article is available online

All solid-state Li batteries (ASBs) are promising to overcome crucial challenges associated with conventional Li-ion batteries, stemming from the organic liquid electrolyte, such as, safety issues due to the flammability and limited energy density due to strong decomposition at high voltages. ASBs with a solid electrolyte offer potential benefits of longer life and safer to operate.[1,2] However, the use of solid electrolyte requires high temperature sintering as an essential step for solid state diffusion, ensuring good interfacial contact between electrode and electrolyte. A good contact ensures better conductivity between these components and improves the mechanical integrity of the complete system. However, the establishment of proper interfacial contact is crucial and mostly an undesirable non-conducting interfacial layer results between the components.[3–7]

Process of sintering has undergone significant improvements over time, particularly in addressing high temperature involvement. Such as, pressure assisted sintering, spark plasma sintering,[8] flash sintering,[9] and ultrafast high temperature sintering[10] etc. These advanced techniques facilitate high heating rates, restrict grain growth and undesirable reactions. Cold sintering is a promising alternative since it combines the effect of external pressure, utilizes aqueous/non-aqueous sintering aids and facilitates the densification at temperatures below 400 °C.[11–13] Literature demonstrates promising results for cold sintered battery materials. Several studies depict that cold sintering with an aqueous sintering aid leaves behind pores and amorphous phases at grain boundaries. Without a suitable post thermal treatment, electrochemical performance is not possible to optimize.[1,14–16] A non-aqueous based cold sintering aid (fused NaOH) if used otherwise can facilitate low temperature densification (in Na ion electrolyte) with better grain boundary conductivity.[17] With these facts in literature, our group put an effort in explaining that aqueous based cold sintering may not always be deleterious to use for Li-ion batteries. Our former, well explained study showed that aqueous phase assisted cold sintering facilitated removal of non-conducting layer from the cathode, $LiMn_2O_4$ (LMO), and resulted in high rate capability electrode.[18]

To continue these studies on cold sintering, this work focuses on cold co-sintering of composite cathode applying $LiMn_2O_4$ (LMO) as electrochemically active phase, while adding LATP as Li^+ conducting phase and carbon black (CB) as electronically conductive phase to further improve electrochemical performance. As electrolyte, our material of choice is $Li_{1.3}Al_{0.3}Ti_{1.7}(PO_4)_3$ (LATP). LATP electrolyte is promising candidate for power sources due to their non-flammable nature, stability in air and possible use of high voltage cathodes. It is known for its high ionic conductivity, mechanical integrity and stability in ambient atmosphere and water.[19] Cold sintering studies on LATP, documented in literature, showed use of aqueous or non-aqueous aids with post thermal treatment resulted in comparatively poor grain boundary regions and overall lower values of conductivity (10^{-5} S cm^{-1}).[20,21] Our main emphasis was to have better understanding of the cold co-sintering of composite cathode and its electrochemical response. Therefore, aqueous phase assisted cold sintering route was adopted for LATP. It might not result an optimum conductivity that could be expected from LATP, but would help to transfer the knowledge to cold co-sintering of composite cathode.

The potential of cold co-sintering of battery electrodes has been shown recently in the work of Joo-Hwan Seo et al.[22] The authors demonstrated a route to co-sinter a complete all-solid-state-battery. They first prepared the composite electrode by mixing $Li_4Ti_5O_{12}$(LTO)/$LiFePO_4$(LFP) with carbon nanofibers (CNF), $LiClO_4$ and polypropylene carbonate (PPC) in acetonitrile. A slurry of LLZO, PPC and $LiClO_4$ was prepared in acetoritrile and drop casted on anode and then dried. They performed cold sintering by putting 7 µl of 9 wt% salt solution of $LiClO_4$ in dimethylformamide (DMF), dropped by micropipette on electrolyte/anode bilayer, applied 300 MPa of pressure and raised the temperature to 100 °C

[z]E-mail: khushnuda@uet.edu.pk

for 1 h of dwell time. However, here we have presented a different approach, relying strictly on cold sintering parameters. The present study discloses many new and interesting details on aqueous phase assisted cold co-sintering of LMO and LATP in the presence of CB. Very first functional composite cathode of its very kind has been prepared and studied. Our results show that there is still a lot of further improvement required to achieve a well-developed, fully functional assembled cell out of the cold co-sintered composite cathode. Nevertheless, our study enables a deeper insight in the remaining challenges for achieving this target.

Experimental Work

LMO was selected as the cathode material and purchased from Marion Technology, France. Powder was characterized for its particle shape, size, purity, electrochemical performance and for its cold sintering behaviour. Details can be found in our previous work.[18] LATP powder was selected as the Li^+ conducting materials and synthesized in house by sol-gel route synthesis, as detailed elsewhere.[19] To study the cold sintering behaviour of pure LATP, the powder was used for these experiments in its calcined state and sintered state, thereby named as LATP_cal and LATP_sin, respectively. LATP_cal powder is the one that was obtained right after the calcination process (600 °C, 3 h, air atmosphere). This calcined powder was then sintered in its loose powder form at over 950 °C, 5 h, air atmosphere and named as LATP_sin. LATP conventionally sintered pellet was also prepared. For that, LATP_cal powder was pressed in the hydraulic press at room temperature at 90 MPa, pressure was released, pellet was removed from the press and sintered at over 950 °C for a dwell time of 5 h. LATP powders were characterized by scanning electron microscopy (SEM, Zeiss Ultra55, Germany), particle size distribution analysis (PSD, particle size analyzer LA950V2, Retsch, Germany) and X-ray diffraction technique (XRD, Advanced Bruker Corporation, Germany using CuKα = 1.5418 Angström). Image analysis using lineal intercept method with the help of ImageJ software was used to calculate the primary particle size of these powders. > 250 particles were considered for each case. Carbon black (Alfa Aesar, Super P Conductive, 99 + % metal basis) was used to enhance the electrical conductivity of electrode material. X-ray photoelectron spectroscopy (XPS- Phi5000 VersaProbe II, ULVAC-Phi Inc., USA) was also performed on cold sintered and conventionally sintered LATP pellets, to study the reduction state of Ti.

For better control over parameters, all cold sintering experiments were performed inside a Field Assisted Sintering Technology/Spark Plasma Sintering (FAST/SPS) device (HP-D5, FCT Systeme, Rauenestein, Germany). A 12 mm diameter tool of TZM (0.50% Titanium, 0.08% Zirconium–99% Molybdenum) alloy was used to facilitate high mechanical pressures up to 400 MPa. Graphite foil (type SIGRAFLEX, SGL Carbon GmbH, Germany) was used between the punch and the powder and between the powder and the die to provide better mechanical, thermal and electrical contact. K–type thermocouple was used and inserted into a small hole drilled in the die. Purpose was to closely monitor the temperature of the sample. 20 °C min^{-1} of heating rate was selected for all cold sintering experiments to provide sufficient time for aqueous phase to leave the powder during the heating cycle of cold sintering. A quantity of ~20 wt% of cold sintering aid was used for all set of cold sintering experiments, based on our previous work.[15,18] For each run, 1 g of powder was poured into the tool die, pre-compacted with 16 MPa of mechanical pressure, cold sintering aid was supplied with the help of micropipette, tool die was closed, inserted in the FAST/SPS machine and program was allowed to run. For each cold sintering cycle, set value of mechanical pressure was applied to the wet powder before the rise in temperature and kept constant during the heating ramp and dwelling time. After that, pressure was released gradually with the cooling cycle. Densification curves are plotted using the data generated from the displacement of the FAST/SPS punches. Every experiment was repeated using the same thermal cycles but without using any powder in the die to subtract the axial expansion of the tool dies.

Before cold co-sintering of cathode and electrolyte, aqueous phase assisted cold sintering of pure LATP was studied to better understand its cold sintering ability. LATP_cal and LATP_sin powders were cold sintered in two separate set of experiments, both at 500 °C, 300 MPa for 20 min of dwell time, using 20 wt% of 1 M aqueous LiOH solution (prepared in house) related to the weight of the respective powder. In a different set of experiments, 20 wt% of 1 M aqueous H_3PO_4 was also used. Cold sintered pellets were characterized by XRD and their fracture surface analysis was made by SEM. Grain sizes (considering at least > 250 grains per condition) were calculated using the lineal intercept method with the help of ImageJ analysis, by a correction factor of 1.56. Pellets were gold sputtered (Cressington 108 sputter coater—TESCAN GmbH, Germany) on both sides and sealed in the Swagelok cells, sputtering and sealing was done in Argon atmosphere. The impedance spectra of the samples were recorded from −20 °C to 80 °C by using a multipotentiostat (VMP-300 Bio-Logic Sciences and Instruments, France) in a frequency range from 3 MHz to 1 Hz and the results were fitted using Z-view software (Scribner Associates Inc., Southern Pines, NC).

Room temperature Raman spectral mapping (INVIA QONTOR, RENISHAW) equipped with a 532 nm laser was performed using a 2400 l·mm^{-1} grating with a laser power of about 5 mW. These spectra were recorded for polished surface cross sections of cold sintered and conventionally sintered LATP. The purpose was to investigate any effect of ion migration, local structural bonding order, imposed by aqueous phase assisted sintering.

For cold co-sintering of LATP and LMO, both powders were mixed by weight in a mortar and pestle. For the different set of experiments, carbon black was added to the powder mixture in varying weight percentages as, 0 wt% CB, 1 wt% and 5 wt%. Mixing, filling and prepressing of powder in the tool die was performed inside the argon filled glovebox. Tool die was removed from the glovebox. Then, 20 wt% of 1 M aqueous LiOH solution was added to the pre-compacted powder and tool die was inserted to the FAST/SPS. Cold sintering was performed at 400 °C, 400 MPa for 1 min dwell time.

Cold co-sintered pellet was removed from the tool die and prepared for electrochemical analysis. Dry grinding was carried out for the pellet for its thickness reduction. A thickness of 0.6–0.7 mm was achieved from coarse grinding (400 grit size) to fine grinding (4000 grit size). Density of these pellets were measured by Archimedes principle and by geometrical means. Theoretical density was calculated by rule of mixture. Active materials loading was ~37 mg cm^{-2} in the cold co-sintered pellet. A thin gold layer as current collector was sputtered on one side of the pellet using a sputter coater (Cressington 108 sputter coater—TESCAN GmbH, Germany). Other side of the pellet was wetted with a polymer electrolyte, a mixture of weight percent of polyethylene oxide (PEO) (Mw = 600000, Aladdin) + 20% bistrifluromethanesulfonimide lithium salt (LiTFSI) (99%, Aladdin), 5% bistrifluromethanesulfonylimide (BMP) (98%, Aladdin) in acetonitrile (99.5%, Aladdin). Wetted pellet was placed on the heating plate and heated to 50 °C for 15–20 min, for improved mechanical and electrochemical performance. Afterwards, a thin Li-metal foil (Alfa Aesar) was attached to the polymer interlayer. The cell was assembled in a Swagelok cell inside the Ar filled glove box.

Electrochemical testing was performed at 50 °C. Galnavostatic cycling was performed in a voltage window of 3.3 to 4.3 V vs Li/Li^+ with a current density of 20 μA cm^{-2} using a multipotentiostat (VMP-300 Bio-Logic Sciences and Instruments, France) combined with a climate chamber (VT 4002EMC, Vötsch Industritechnik GmbH, Germany). The data were evaluated by EC-lab software (BioLogic Sciences Instruments, France).

Results and Discussion

Cold sintering of LATP with aqueous sintering aids.—LATP powder was thoroughly investigated for its response towards same cold sintering parameters as were used for LMO in our former work.[18] PSD analysis showed comparatively large size agglomerates in LATP_sin powder as compared to LATP_cal powder as can be seen in table S 1. Ultrasonic agitation was used for breaking the agglomerates. The agitation time was varied between 0 and 15 min, enabling to break agglomerates but to a limited extent. After 15 min of ultrasonic agitation, both powders had almost similar size of agglomerates as ∼4 μm and ∼5 μm for LATP_cal and LATP_sin, respectively. These large size agglomerates apparently may resist hard to the applied uniaxial pressure for cold sintering process.[23] Nevertheless, these large size agglomerates assisted in cold co-sintering, as would be explained shortly later.

SEM analysis shown in Fig. 1 revealed for both powders the size difference between the primary powder particles and their agglomerates. Fine size of 0.34 ± 0.28 μm was observed for LATP_cal powder (Table S1). LATP_sin powder was observed to have a similar size range of 0.49 ± 0.25 μm.

Figure 2a shows the densification curves for the cold sintering of LATP_cal powder indicating the cold sintering parameters of 500 °C, 300 MPa, 20 °C min^{-1}, 1 min dwell time in different nature of aqueous cold sintering conditions. Absence of aqueous aid, use of 1 M aqueous LiOH solution and 1 M aqueous H_3PO_4 solution resulted in ∼65%, ∼85% and ∼95% RD. Cold sintered samples prepared from LATP_cal powder turned blue after cold sintering while cold sintered pellet prepared from LATP_sin powder and the one that was prepared without any aqueous aid stayed white in colour. The values of the initial densities can also be read from the starting points of these densification curves as ∼61%, ∼48% and ∼56% RD, respectively. Figure 2b presented the variation in gas pressure inside FAST/SPS chamber during respective cold sintering cycles. Similarly, Figs. 2c and 2d were plotted for LATP_sin powder for its cold sintered densification in the presence of 1 M aqueous LiOH solution and associated gas pressure variation (Fig. 2d), respectively.

Different humps in gas pressure variation curves in Figs. 2c, 2d hint on different nature of gaseous products released during cold sintering cycle, disturbing the set vacuum conditions. DTA/TGA analysis coupled with mass spectrometer was also carried out for the same thermal cycles (Fig. S1a, S1b). Figure S1a S1b differentiated the behaviour of LATP in the presence and absence of aqueous aid. Very negligible mass loss in the absence of aqueous aid (Fig. S1a) and an appreciable mass loss in the presence of aqueous aids were observed (Fig. S1b). Mass spectrometer confirmed the release of gaseous species (OH, H_2O, CO_2, H_3O, NO, CH_3O) in the absence of any aqueous aid starting after 50 °C. However, the use of the aqueous aid caused the release of gaseous products starting from 30 °C, with their nature being H_2O, CO_2, OH and H_3O. Figure S 1 c shows the response of our cathode material, LMO, towards both aqueous aids. Very slight weight loss in the presence of 1 M aqueous LiOH solution and comparatively higher loss in the presence of 1 M aqueous H_3PO_4 solution were observed in this case. LMO undergoes dissolution in the presence of H^+ concentration and therefore should not be used in acidic environments.[24]

Sample sintered without any aqueous aid showed a higher value of initial density. In Fig. 2a, this could be interpreted as the absence of liquid bridges that may otherwise offer higher resistance and maintain a larger interparticle distance.[23,25–27] The difference of initial densities between samples, cold sintered using both aqueous phases could be interpreted according to the possible difference of the use of distinct aqueous phases.[28] Removal of gaseous species as could be seen in Figs. 2b, 2d, indicating the possible surface cleaning and possible pores formation in the cold sintered pellets.[18,29] Here large size agglomerates also assisted in gases to get released from the pellets, by facilitating gaps between the particles.

Detailed XRD analysis was not able to discriminate the influence of blue colour (Fig. 3) in the samples. $AlPO_4$ and TiO_2 appeared as secondary phases for LATP_cal and LATP_sin powder (Figs. S2 a

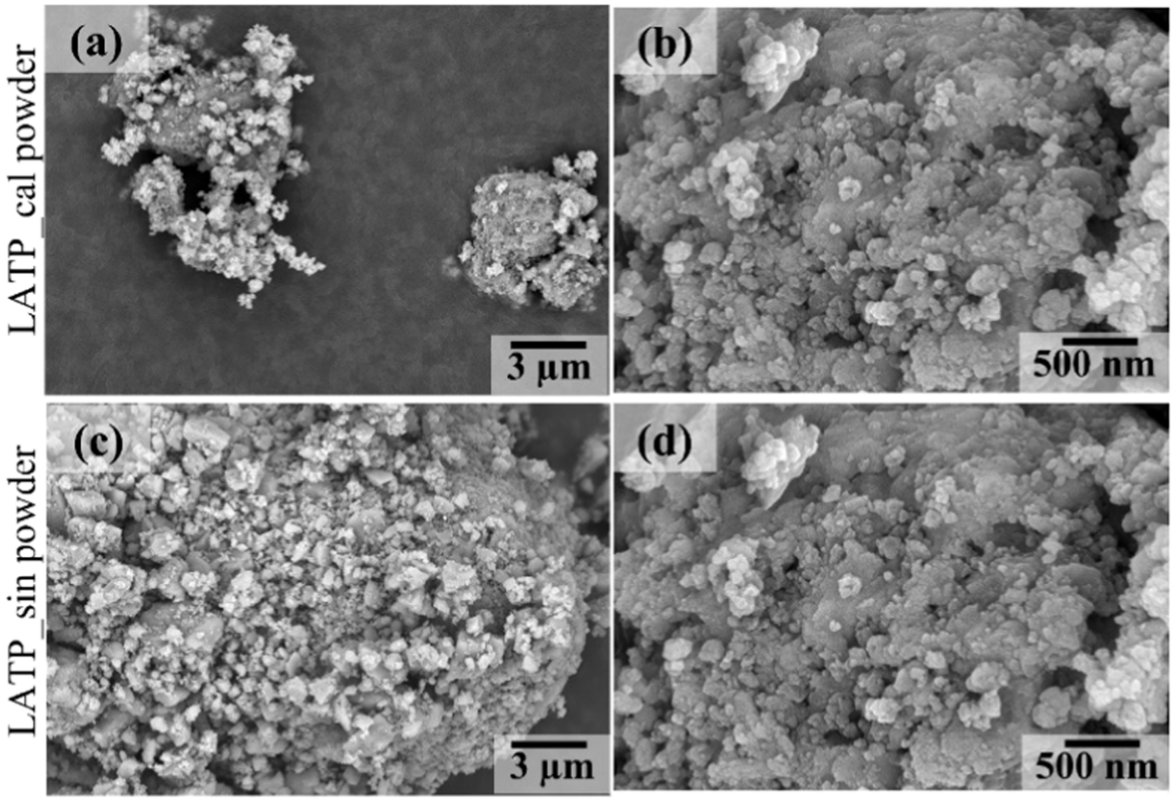

Figure 1. SEM images of (a, b) LATP_cal (achieved after calcination at 600 °C, 3 h, air) and (c, d) LATP_sin powders (achieved after sintering the loose powder at 950 °C, 5 h, air).

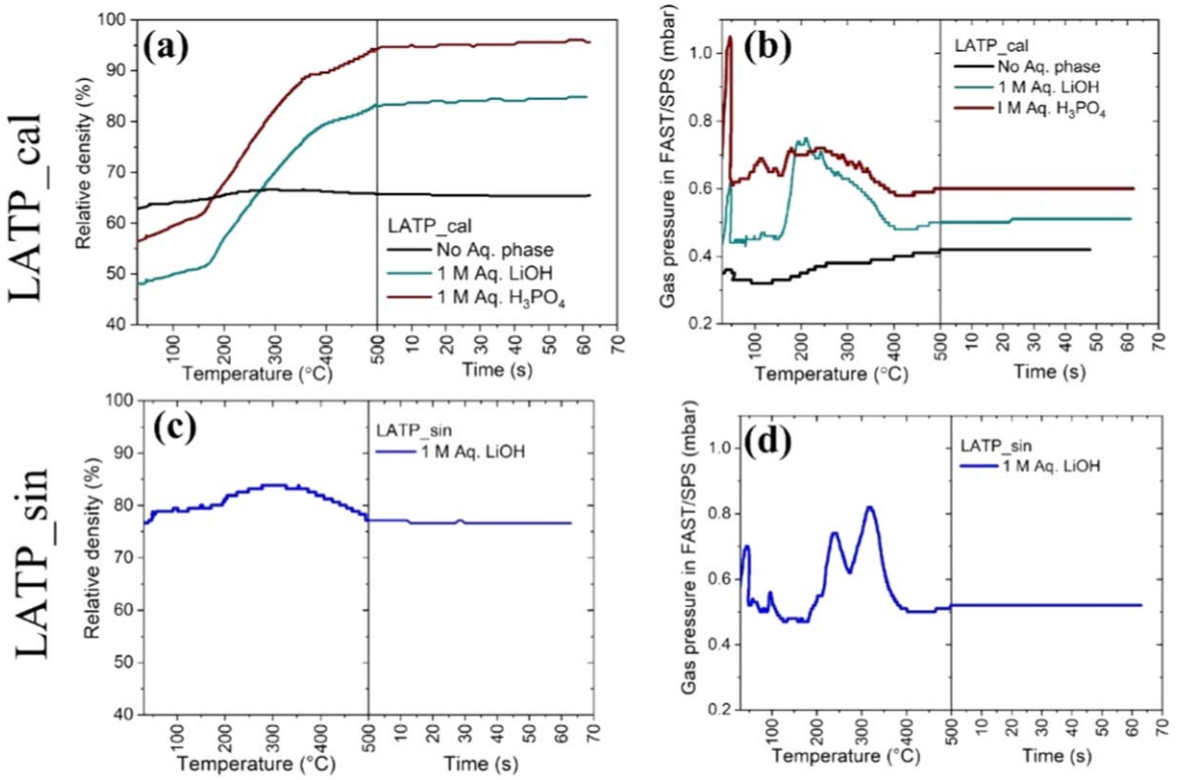

Figure 2. Cold sintered densification curves and gas pressure variation curves for (a, b) LATP_cal powder and (c, d) LATP_sin powder, respectively.

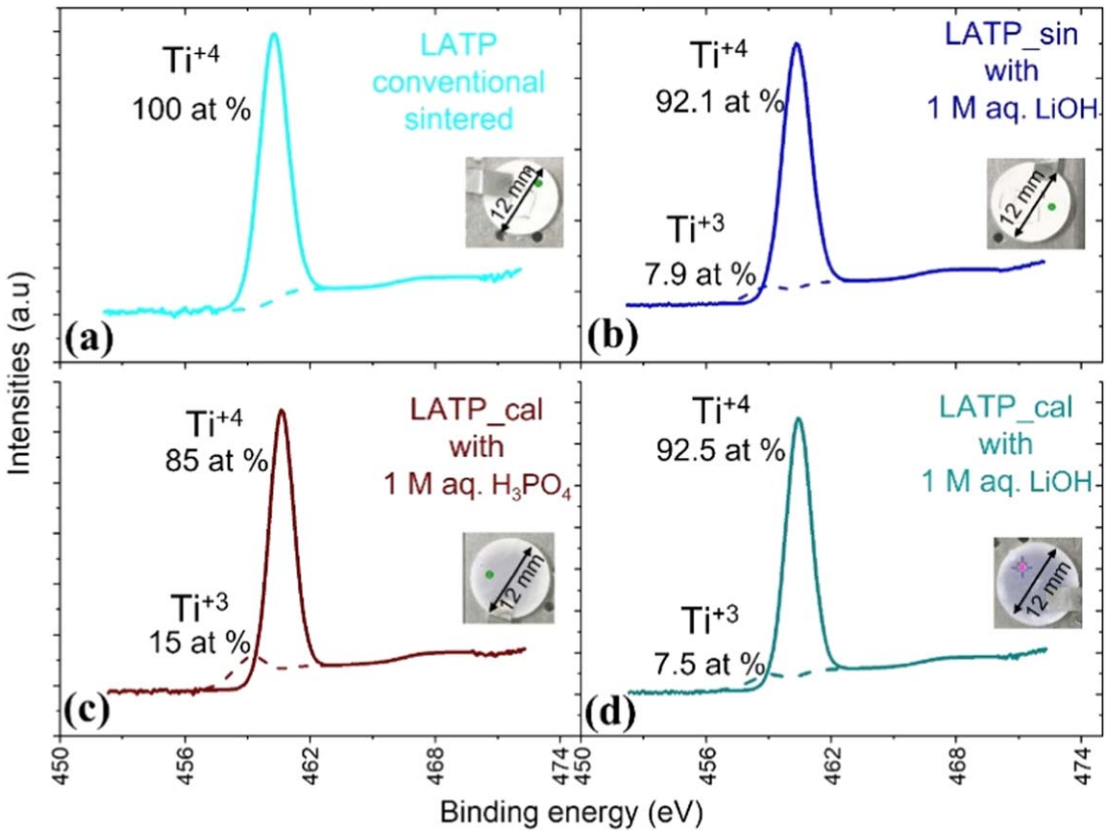

Figure 3. XPS spectra of Ti showing 2p signals with 2p 3/2 fitting for the samples: (a) LATP pellet prepared by conventionally sintering of LATP_cal powder without using any aqueous aid, (b) Cold sintered pellet prepared by LATP_sin powder using 1 M aqueous LiOH solution, (c) Cold sintered pellet prepared by LATP_cal powder using 1 M aqueous H_3PO_4 solution and (d) Cold sintered pellet prepared by LATP_cal powder using 1 M aqueous LiOH solution. (Conventional sintering conditions: over 950 °C, 5 hr dwell time, initial pressure of 90 MPa, heating rate 5 °C min^{-1}. Cold sintering: 500 °C, 20 wt% aqueous solution, 1 min dwell time, 300 MPa of uniaxial pressure constant during heating and dwell time, 20 °C min^{-1} heating rate).

S2b). These phases normally route back to different nature of precursors composition or high temperatures used for calcination and sintering.[30,31] Aqueous phase assisted cold sintering pellets were contaminated with further secondary phases as $LiZr_2(PO_4)_3$ in LATP_cal (with 1 M aqueous LiOH solution), $LiTiPO_4$ in LATP_sin (with 1 M aqueous LiOH solution), as well as $AlPO_4$ and $LiZr_2(PO_4)_3$ in LATP_cal (with 1 M aqueous H_3PO_4 solution). These secondary phase peaks can be observed in Figs. S2c–S2e respectively and in Fig. S2f. Reduction in the peak intensities for cold sintered samples with respect to the starting powders hint on loss of crystallinity after cold sintering. This observation corresponded well the TEM characterization of cold sintered LATP by Y. Liu et al.[20]

XPS data in Fig. 3 provided a detailed spectrum of Ti 2p doublet line. Peak fit analysis of Ti $2p_{3/2}$ revealed two components at comparatively low binding energy of 459.1 eV and a bit higher binding energy of 460.4 eV, representing Ti^{+3} and Ti^{+4} oxidation states, respectively. Low binding energy component was not observed in LATP conventionally sintered. Here, all Ti atoms were in the Ti^{+4} oxidation state (100 at%) resulting in the white color of the sample (Fig. 3a). LATP_sin with 1 M aqueous LiOH solution had 7.9 at% Ti^{+3} and 92.1 at% of Ti^{+4} (Fig. 3b). LATP_cal with 1 M H_3PO_4 had maximum of 15 at% Ti^{+3} (Fig. 3c) and LATP_cal with 1 M aqueous LiOH solution were observed to have minimum of 7.5 at% Ti^{+3} (Fig. 3d). Analogous to the Ti^{+3} existence in the respective samples the blue colour is shown by the inserted images in the Fig. 3.

LATP based electrolyte materials are known to get reduced from Ti^{+4} to Ti^{+3} on interacting with Li metal as an anode. This reduction becomes visible as blue colour of the sample.[32–36] In the present case aqueous solutions played the same role. Acidic phase being a good donor of proton caused more reduction than that of the basic phase.

Figure 4 displays SEM images for fracture surfaces of cold sintered LATP. Finer particles existed in LATP_cal powder (Figs. 4a, 4c) than LATP_sin powder (Figs. 4e, 4f). Cold sintered pellets, LATP_cal with 1 M aqueous LiOH solution and LATP_cal with 1 M aqueous H_3PO_4 solution, showed good particle to particle contacts in the fracture surface analysis but with prevalent micro cracking (Figs. 4b, 4d). Cracking is comparatively more dominant in LATP_cal with 1 M aqueous LiOH solution, this could be the reason for comparatively lower densification in this sample as that of LATP_cal with 1 M aqueous H_3PO_4 solution. Microcracking is known to occur in LATP at high temperature sintering because of the difference in coefficient of thermal expansion of LATP crystals and undesirable secondary phases ($AlPO_4$). Microcracking has an influential negative effect on the ionic conductivity and mechanical stability and could be reportedly reduced with controlled grain growth, such as with low temperature sintering.[37,38] In the present studies, high temperature did not seem to be an issue but the use of high uniaxial pressure. Previously, pressure assisted LATP sintering had been documented to result in microcracking because of the use of high mechanical pressures.[39] Contrarily, LATP_sin cold sintered with 1 M aqueous LiOH solution showed incomplete densification with very large triple points between the particles.

Figure 5a shows the Arrhenius plot of the total ionic conductivity of three cold sintered LATP samples, LATP_cal with 1 M aqueous LiOH solution, LATP_cal with 1 M aqueous H_3PO_4 solution and LATP_sin with 1 M aqueous LiOH solution with almost 85, 95 and 75% RD, respectively. It must be kept in mind at this point that these values of relative densities must be considered as approximate values. Since the role of secondary phases cannot be excluded. For the calculation of the total ionic conductivity electrochemical impedance spectroscopy was performed and equivalent circuit model for data fitting were drawn. One example is shown Fig. 5b. One semicircle was observed as determined by the intersection of Nyquist plot with x-axis at low frequency, thus total conductivity was calculated by R0 + R1, where R0 is related to bulk conductivity and R1 is related to the grain boundaries. An exceptionally large contribution from grain boundary resistance would be expected to influence the overall performance of full cell. The total conductivity of the samples at 25 °C were measured as 1.4×10^{-6} S cm^{-1}, 2.7×10^{-6} S cm^{-1} and 4.9×10^{-6} S/cm for, LATP_cal with 1 M aqueous LiOH solution, LATP_cal with 1 M aqueous H_3PO_4 solution and LATP_sin with 1 M aqueous LiOH solution cold sintered samples, respectively. The total conductivity calculated for conventionally sintered LATP was 0.5×10^{-3} S cm^{-1}. Experimental data collected at different temperatures were fitted according to the Arrhenius equation:

$$\sigma T = Ae^{-\frac{E_a}{k_B T}}$$

Here, σ is the conductivity, T is the absolute temperature, A is a pre-exponential factor, E_a is the activation energy and k_B is the

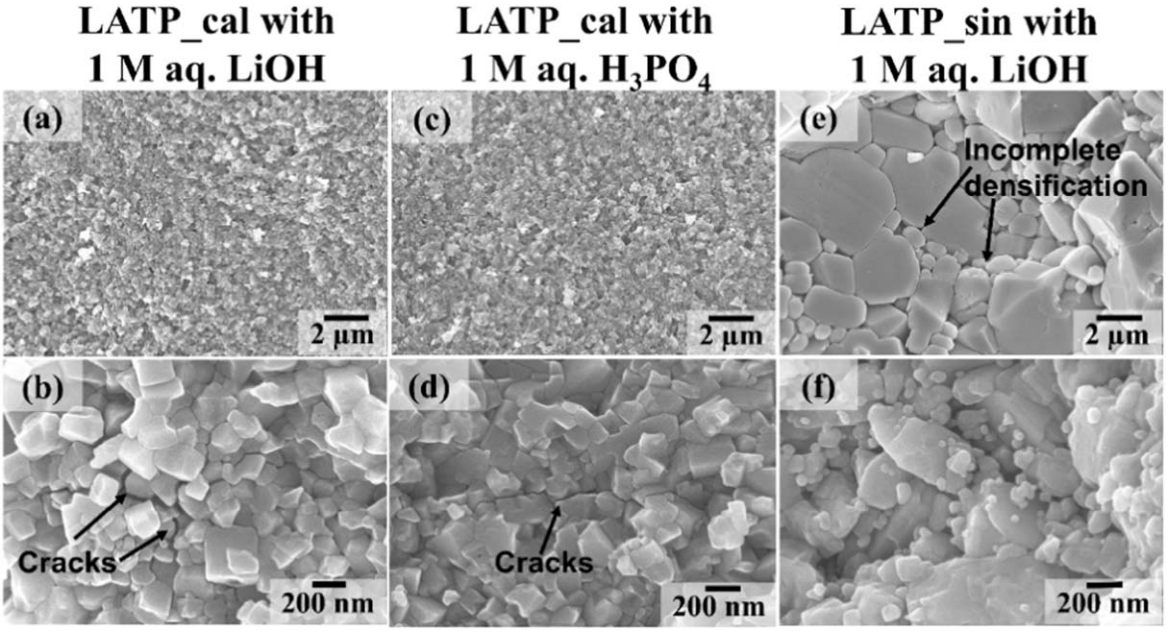

Figure 4. SEM images of fracture surfaces for cold sintered LATP (a, b) LATP_cal with 1 M aqueous LiOH solution, (c, d) LATP_cal with 1 M aqueous H_3PO_4 solution, (e, f) LATP_sin with 1 M aqueous LiOH solution.

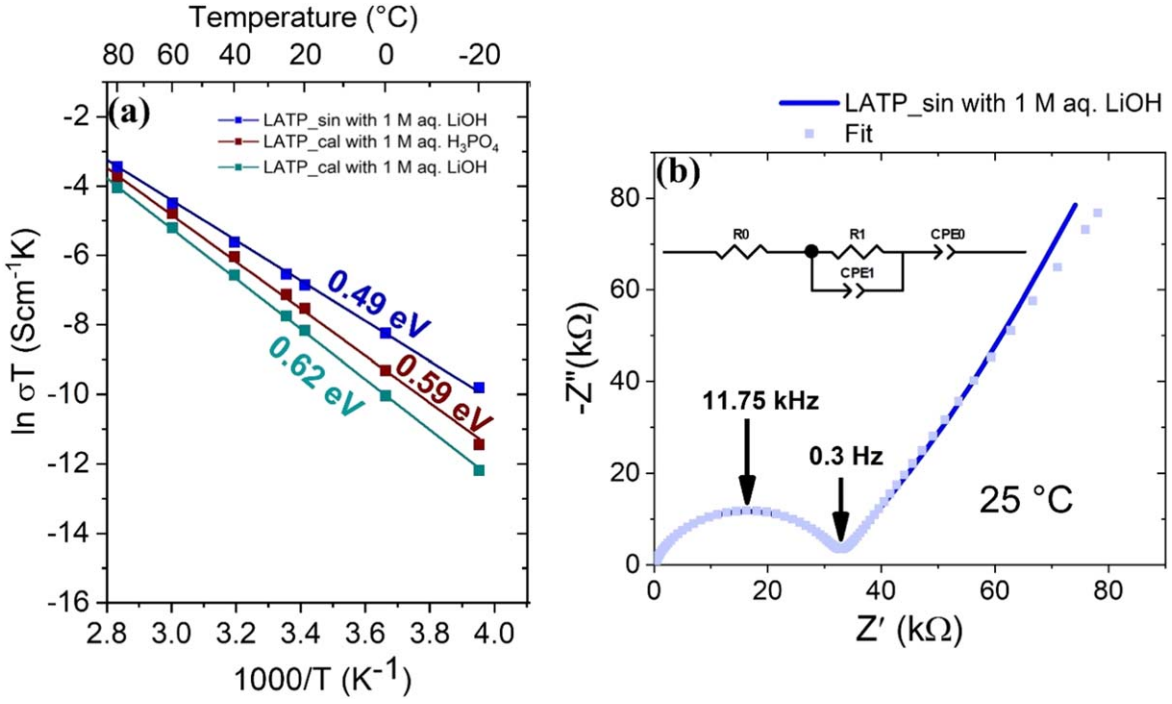

Figure 5. (a) Arrhenius plot of the total conductivity of cold sintered LATP samples in the presence of respective aqueous aids. (b) At 25 °C, Nyquist plot (open circuit) and the simulated data (solid line) of one of the samples (LATP_sin with 1 M aqueous LiOH solution) with the equivalent circuit are shown in the inset, R and CPE represent resistance and constant phase element, respectively.

Boltzmann constant. For this expression, E_a values for the given samples were calculated as 0.62 eV, 0.59 eV and 0.49 eV, respectively. While 0.37 eV was calculated for conventionally sintered LATP.[19] These values have been summarized in Table I for comparison.

Our cold sintered samples showed highest density in the presence of aqueous H_3PO_4 solution when calcined LATP was used, although the value of activation energy is highest for the given case. Lowest value of activation energy was calculated for cold sintered LATP sample while using LATP sintered powder and LiOH aqueous solution. The dominant effect on the conductivity values preferably came from higher grain boundary concentration, when LATP calcined powder was used. LATP_cal with 1 M aqueous LiOH solution and LATP_cal with 1 M aqueous H_3PO_4 solution almost had similar grain size range as 146 nm ± 74 and 146 nm ± 45, respectively. However, LATP_sin with 1 M aqueous LiOH solution had grain size of 1.72 μm ± 1.25 and apparently better crystallinity and lesser distortion at grain boundaries (Fig. S2c). Comparison of cold sintered sample and conventionally sintered sample elaborated the combine effect of grain size and refined grain boundaries towards total conductivity. Cold sintered LATP as documented in literature, displayed a maximum total conductivity of 8.04×10^{-5} S cm^{-1} with 0.37 eV of activation energy, not to forget the contributing role of post thermal treatment at 650 °C for 2 h in this case.[20] Their results showed very close values of relative density and activation energy for cold and conventional sintered samples, yet one order difference in the values of conductivity. This again endorsed the role of grain sizes towards conductivity, with cold sintered samples having small grains.[20] In another work, cold sintered LATP, with the use of different nature of sintering aids, displayed a maximum value of conductivity as 10^{-4} S cm^{-1} but with the assistance of post annealing step.[41] A secondary low temperature resistant phase can also be used to offer sintering of LATP at reduced temperature, offering up to 95% densification and 10^{-4} S cm^{-1} of the conductivity.[42] Our LATP_sin with 1 M aqueous LiOH solution sample was able to get to 75% RD despite having large grain sizes. On the other hand, samples prepared from LATP calcined powder were not post thermal treated and showed poor response of grain boundary conductivity. In the present study, any attempt of doing post thermal treatment broke the pellet into small fragments or caused delamination. Inhomogeneity in the cold sintered pellets due to the presence of pores and secondary phases, as explained earlier, could have caused this problem.

To investigate the role of water towards conductivity, a detailed Raman spectra comparison was carried out. Analysis was kept to the samples cold sintered using 1 M aqueous LiOH, since LATP was to be sintered with LMO for composite formation. Figure 6 showed the vibrational spectra for given cold sintered LATP samples in comparison to conventionally sintered LATP sample. Raman modes were observed between 100 to 1000 cm^{-1} and are consistent with the reported values in the literature.[43–46] Higher frequency modes were examined to investigate the presence of residing water.[46] Raman spectra for cold sintered samples almost match with that of conventionally sintered samples as can be seen in the Fig. 5. The peak appearing at ∼780 cm^{-1}, for LATP conventional sintered and LATP_sin with 1 M aqueous LiOH solution represents $LiTiOPO_4$, an impurity phase route back to synthesis process.[45,47] The most intense peak at ∼1016 cm^{-1} is apparent for all the samples, denoting the stretching mode of phosphate ion.[43,45] A noticeable shoulder for this intense peak is evident only for LATP_sin with 1 M aqueous LiOH solution sample, as compared to conventionally sintered sample. This shoulder denotes the possible replacement of Li^+, probably because of aqueous phase assisted sintering.[43] Higher frequency peaks are showing a visible pattern for LATP_sin with 1 M aqueous LiOH solution sample but almost no peaks for other samples. Dashjav et al., found out in their detailed analysis that LATP was having better conductivity after being emersed in water with clear identification of residual water at grains and grain boundaries as ∼1640 cm^{-1} and ∼1580 cm^{-1} spectral regions.[46] These weak bands are apparent in Fig. 6 for LATP_sin with 1 M aqueous LiOH solution and could be the prominent reason for better conductivity of this cold sintered pellet. LATP_conventional sintered sample did not have any residual water source, so it did not show such spectral variation. LATP_cal with 1 M aqueous LiOH solution did not show these spectral regions despite having the same nature and quantity of aqueous phase addition. Sintered particle thus

Table I. Effect of sintering parameters on the densification, total conductivity (at 25 °C) and calculated values of activation energy for LATP samples as compared to documented values in the literature.

	LATP samples	Relative density (%)	Total conductivity at 25 °C (S/cm)	Grain size	Activation energy (eV)	Comparison with the literature
1	LATP_cal with 1 M aqueous LiOH solution	85	1.4×10^{-6}	146 nm ± 74	0.62	Our work
2	LATP_cal with 1 M aqueous H_3PO_4 solution	95	2.7×10^{-6}	146 nm ± 45	0.59	
3	LATP_sin with 1 M aqueous LiOH solution	75	4.9×10^{-6}	1.72 μm ±1.25	0.49	
4	Conventionally sintered sample	97	0.5×10^{-3}	> 1 μm	0.37[19]	
5	LATP sintered at 1000 °C, 2 h	95	1.51×10^{-4}	μm sized	0.37	20
6	LATP cold sintered at 120 °C, 1 h then 650 °C for 2 h using acid	93	8.04×10^{-5}	nm to μm sized	0.37	
7	LATP at 1000 °C (spark plasma sintering)	96	1×10^{-3}	—		38
8	Single crystal LATP		5.1×10^{-3}	—	0.20 eV	19, 40
9	Cold sintered at 200 °C, 1 h dwell time, 20 wt% H_2O, post annealing at 800 °C for 1 h	95	1.55×10^{-4}			41
10	Cold sintered at 200 °C, 1 h dwell time, 20 wt% acetic acid	94	0.82×10^{-5}			
11	Cold sintered at 200 °C, 1 h dwell time, 3.2 wt% lithium acetate	88	9.5×10^{-7}			
12	Reduced temperature sintering for LATP using Li_2Co_3 (at 840 °C), Li_3PO_4 (at 750 °C) and Li_3BO_3 (at 800 °C) as sintering aids, respectively	95.5%, 92.4%, 92.8%, respectively.	3.6×10^{-4}, 0.8×10^{-4}, 2.9×10^{-4}, respectively.			42

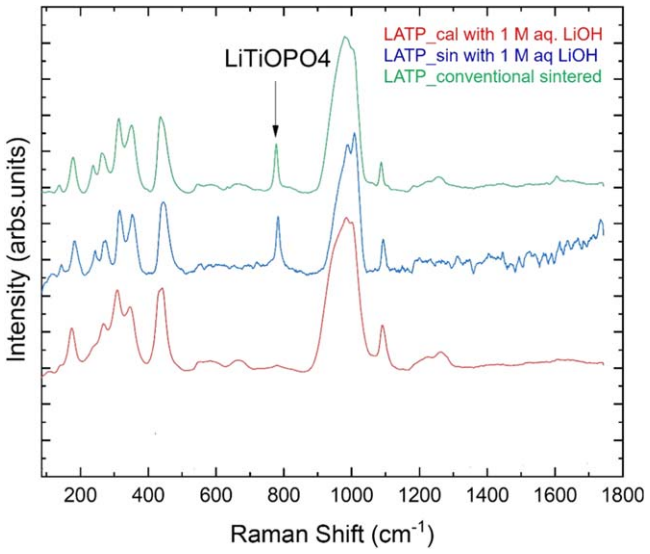

Figure 6. Raman spectra of cold sintered LATP samples in comparison to conventional sintered LATP.

probably provided better assistance for water to reside and play towards conductivity.

Cold co-sintering of LMO/LATP/CB composite cathode with aqueous sintering aid.—The sample, LATP_sin with 1 M aqueous LiOH solution was selected to perform cold co-sintering with LMO and CB because LATP_sin powder displayed better crystallinity, lower activation energy and better Li^+ conductivity. 1 M aqueous LiOH solution was better choice as sintering aid for this study to avoid acidic medium. LMO undergoes Mn dissolution in an H^+ rich environment with pH < 7.[18,24] Temperature for cold co-sintering of the mixed LATP/LMO/CB cathode was kept lower than for pure LATP, since maximum of gas pressure variation was observed till 400 °C with no appreciable increase in densification (Fig. 2).

Preliminary results were achieved omitting CB as conducting phase and cold co-sintering of LMO powder and LATP_sin powder, using 400 MPa pressure, 400 °C and 20 wt% 1 M aqueous LiOH solution. Figure 7a shows the densification curve with ∼85% RD after cold sintering cycle and Fig. 7b demonstrates its respective gas pressure variation inside the FAST/SPS chamber. First hump in Fig. 7b represented the removal of excessive aqueous phase, while second hump could be related to the removal of gaseous species as were observed/explained earlier in our former work of cold sintering of LMO.[18] Figures 7c–7e show the comparative XRD analysis of cold co-sintered pellet with LMO powder and LATP_sin powder, respectively. $AlPO_4$ as the secondary phase was observed in cold co-sintered pellet. This phase is known to appear in LATP at high temperatures (> 950 °C) treatment due to loss of Li in the form of Li_2O. This leads to cracking because of difference in co-efficient of thermal expansion and lower the value of conductivity.[7,38,48] For this reason, it has been suggested in literature to preferentially use low temperature sintering for LATP. Present studies showed $AlPO_4$ and TiO_2 peaks as secondary phase (Fig. 7c) despite low temperature sintering, hint on the incongruent dissolution of Li ions due to the use of aqueous phase assisted sintering. This cold co-sintered pellet showed a conductivity of 1.6×10^{-5} S cm^{-1}.

CB as the conducting phase was added to LMO and LATP_sin powder in the ratio of 1 and 5 wt%. Powders were mixed together, then filled in the FAST/SPS die as the schematic in Fig. S3. Cold co-sintering was performed using the same parameters used before and densification curves showed a final RD of ∼79% and ∼82% for cold co-sintered composite cathodes (sample code CCSCC) with 1 wt% CB and 5 wt% CB, respectively (Fig. 8a and Table S2). Here again gas pressure variation curves for both samples showed an observable hump in two regimes of temperatures below 50 °C and in the range of 200 to 250 °C (Fig. 8b). These humps resulted due to the removal of gaseous species as a reaction between powder surfaces and aqueous phases.[18,29] The sample with 1 wt% CB always showed short circuiting, here the electrical conductivity could be dominant

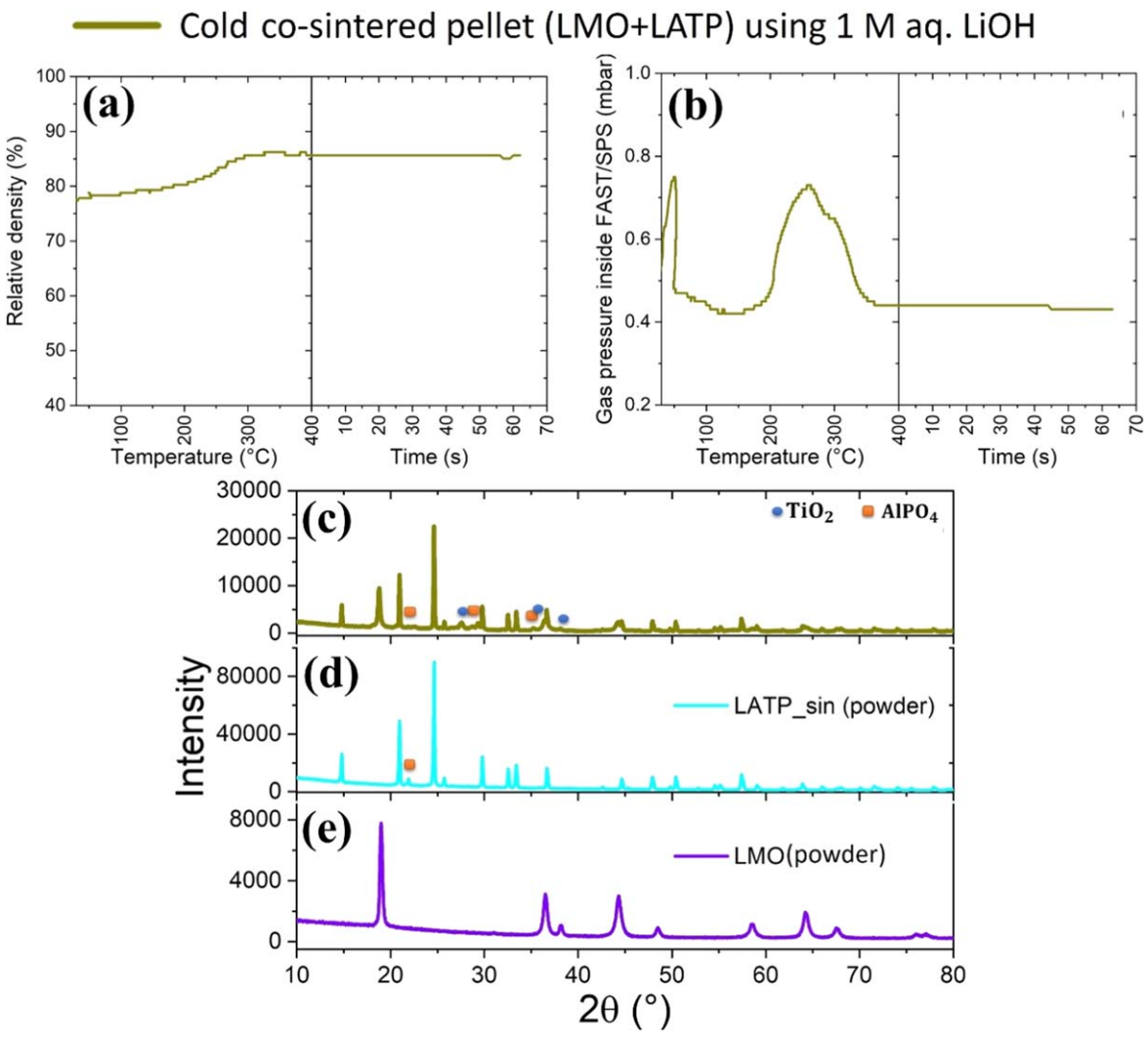

Figure 7. (a) densification curve and (b) gas variation curve for cold co-sintering of LATP_sin powder with LMO powder at 400 °C, 400 MPa, 1 min dwell time using FAST/SPS. XRD analysis of (c) cold co-sintered pellet prepared form LATP_sin powder and LMO powder with a comparison to (d) LATP_sin powder and (e) LMO powder.

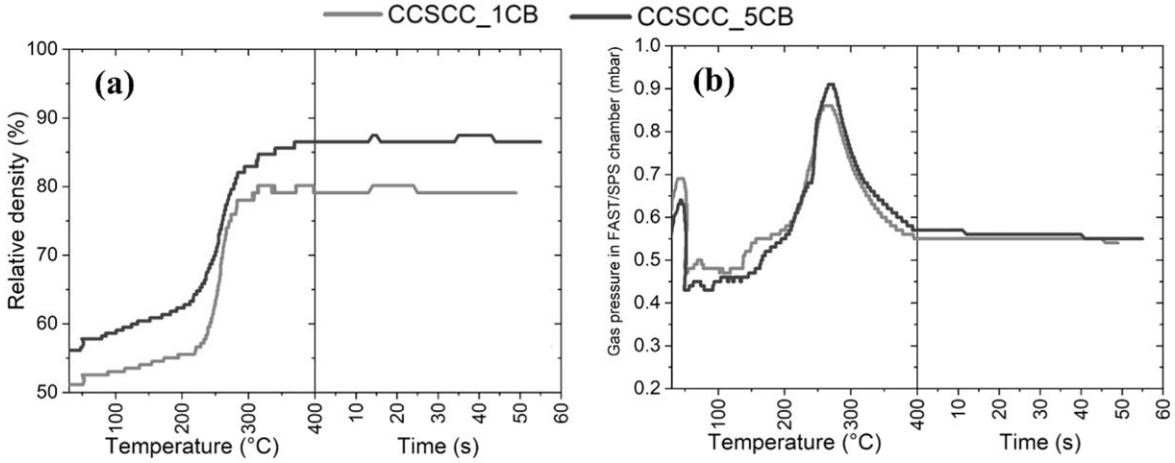

Figure 8. (a) densification curves for CCSCC while using FAST/SPS (b) gas pressure variation curves inside FAST/SPS during cold sintering of CCSCC.

by either of the components, CB or LMO, as per their relative content.[49] While the sample with 5 wt% CB showed a value of 3.1 mS cm^{-1}.

XRD analysis carried out for these cold co-sintered pellets displayed dominant peaks of LATP and LMO and carbon with a number of secondary phases like $LiMnPO_4$ (orthorhombic), $AlPO_4$

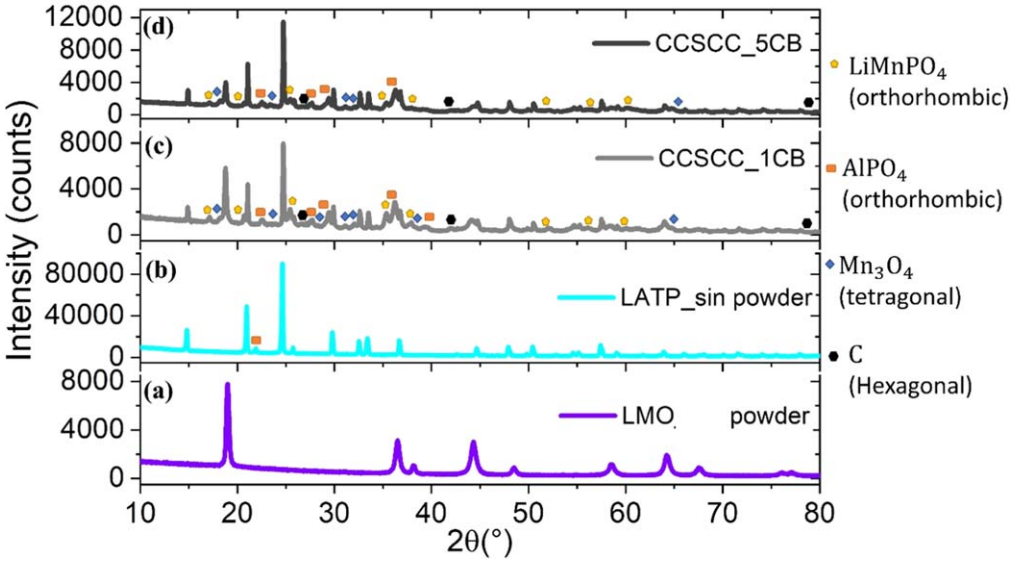

Figure 9. Comparative XRD analysis of (a) LMO powder (b) LATP_sin powder (c) Cold co-sintered composite cathode prepared using 1 wt% CB (CCSCC 1CB), (d) Cold co-sintered composite cathode prepared using 5 wt% CB (CCSCC 5CB).

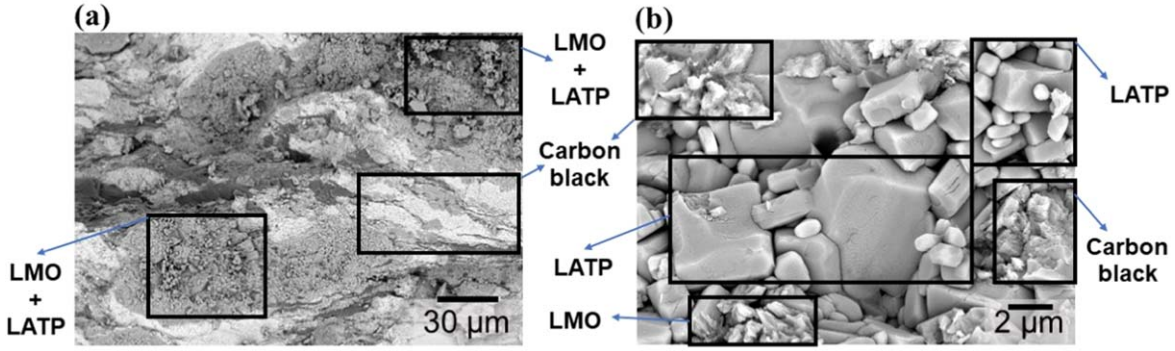

Figure 10. SEM analysis of (a) cross section of CCSCC 1CB and (b) fracture surface of CCSCC 1CB.

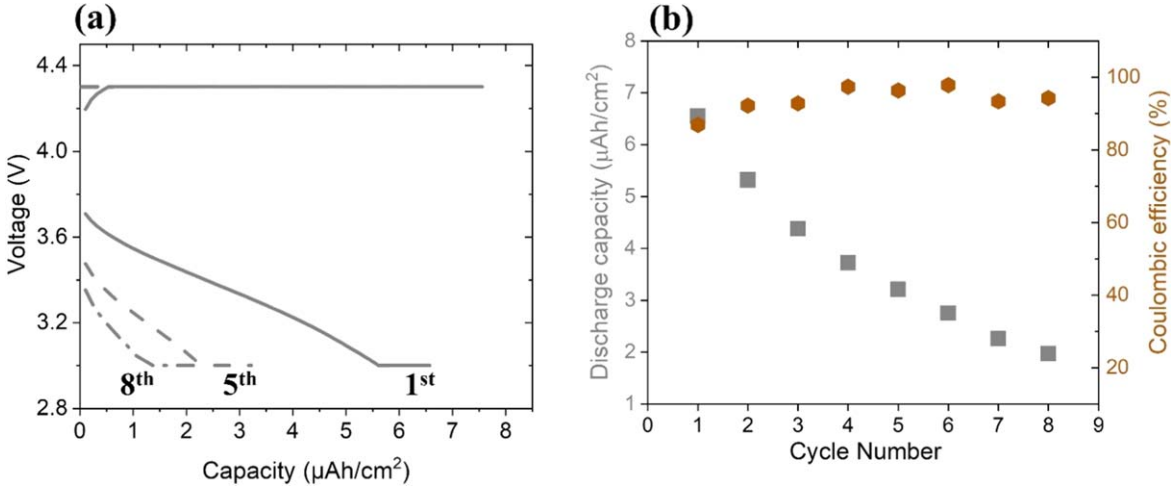

Figure 11. Electrochemical performance of cold co-sintered composite cathode (CCSCC_1CB) within the voltage window of 3.3 V–4.3 V vs Li/Li^+ using current density of 20 μA cm^{-2} showing (a) Voltage profiles for 1st, 5th and 8th cycles, (b) Discharge capacity and coulombic efficiency for prolonged cycling.

(orthorhombic) and Mn_3O_4 (tetragonal), as can be seen in Fig. 9. SEM analysis of CCSCC_1CB in Figs. 10 a and 10b showed well distributed LMO, LATP and CB powders in its polished cross section and fracture surfaces, respectively.

When compared to Fig. 7c, these phases resulted possibly due to the chemical reactions between aqueous phase and carbon black. Aqueous phase caused the interdiffusion and resulted in the formation of $LiMnPO_4$, an electrochemically active compound.

There is a possibility, that carbon black developed dangling bonds—highly reactive coordinative unsaturated carbon atoms on their surface due to milling. In the presence of heat, water vapours might develop and allow the reactive carbon surface to hydroxylate which then react with transition metal or phosphate ions and offered as oxygen bridges. These likely Mn–O between carbon black displayed themselves as Mn_3O_4 (tetragonal) also known as haussmanite could facilitate a good electrical contact between carbon black and $LiMnPO_4$, as well as with LMO.[50]

Cold co-sintered pellet (CCSCC_1CB) was assembled in the Swagelok cell and voltage profile was studied, as can be seen in Fig. 11a. Figure 11b shows the discharge capacity for maximum cycles displayed by the cell with respective coulombic efficiencies. The cell delivered a very low discharge capacity of merely 5.59 μA cm^{-2} with a continuous decrease to a value of 1.22 μA cm^{-2} at its 8^{th} cycle, however the coulombic efficiency was calculated to be almost $>$ 90% for each cycle. Even though polymer electrolyte was used that could penetrate the open pores and contribute towards supressing the overall resistance, certain factors remain dominant, mainly determining the cell behaviour. Overall low performance also hints on insufficient porosity limiting the penetration of polymer electrolyte into the cold co-sintered pellet. This very low capacity could also be explained as a response of higher grain boundary resistance offered by both, active material as well as electrolyte material. Presence of impure phases, exceptionally low value of LATP conductivity and higher value of working potential for the electrolyte could also be among the most probable reasons behind this manifestation. However, further optimization of composite cathode processing and a more detailed electrochemical testing with subsequent microstructure analysis are necessarily required for better understanding.

Conclusions

In our previous study,[19] we demonstrated high-rate capability LMO as well-performing Li battery electrode after being treated with aqueous phase assisted cold sintering. In the present work, we targeted to transfer this promising result for the cold co-sintering of a composite cathode containing LMO for Li^+ storage, LATP for Li^+ conduction and CB as the electronic conducting phase. To better understand the cold sintering behaviour of this composite cathode, we started our study with cold sintering of pure LATP complementing the findings from our previous study on LMO.[19] Cold sintering of LATP showed 85% RD using 20 wt% 1 M aqueous LiOH solution with impurity phases as confirmed by XRD. This cold sintered LATP also presented slight Ti^{+4} reduction to Ti^{+3}, as observed in XPS, and residual water was observed in Raman spectra. Only comparatively low total ionic conductivities (2.7×10^{-6} Scm^{-1}) due to a high grain boundary resistivity and high values for the activation energy (0.62 eV) were achieved compared to conventionally sintered LATP. These findings confirm the problems associated with the use of aqueous phase cold sintering. Present study focussed on the cold co-sintering of LMO/LATP/CB and associated challenges. While our former study demonstrated that cold sintering can be used to improve the performance of LMO based cathodes, the transfer of this approach for the cold sintering of a LMO/LATP/CB composite cathode did not give appreciable results under similar cold sintering conditions. XRD analysis showed very small peaks for TiO_2 and $AlPO_4$, secondary phases usually formed at higher sintering temperatures, here even appearing at low temperatures applied for cold co-sintering of LMO and LATP. Introduction of CB triggered side reactions and became the reason for further secondary phases (conducting and non-conducting by nature) to appear. Approximately 85% RD density was achieved for the cold co-sintered pellet. For electrochemical characterization of the cold co-sintered cathode, a Swagelock cell with polymer electrolyte (PEO + 20% LiTFSI, +5% BMP in acetonitryle solution) and Li counter electrode was assembled. Electrochemical characterization of the Swagelok cell reveals very low values for areal capacities, 5.59 μA cm^{-2} for the first cycle, and then rapidly degrading to 1.22 μA cm^{-2} after nine cycles. In conclusion, this study delivered a first insight into cold co-sintering of composite cathode based on LATP for all-solid-state Li batteries, highlighting the challenges and can thus provide orientation for future research directions.

Outlook

It is expected that cold co-sintering can be improved based on these potential candidates with the use of optimal Li^+ conducting phase as cold sintering aid for better grain boundary conditions, in terms of conductivity and inter-chemical reactions. This has to be investigated in detail for both materials, LATP and LMO, since both have different response in the given cold co-sintering conditions. In addition the role of CB needs to be understood with much deeper understanding with possible substitution of cold sintering aid or CB, itself. It is also highly recommended to study an alternative liquid/polymer electrolyte or perhaps simply a solid electrolyte, if porosity can be controlled, to enhance the electrochemical character of the cold co-sintered composite cathode.

Acknowledgments

Khushnuda Nur acknowledges the support from University of Engineering and Technology, Lahore, Pakistan and also the funding from the German Research Foundation (DFG) through projects GU993/ 10. Financial support by the "Bundesministerium für Bildung und Forschung" (Federal ministry of education and research), Germany, under projects no. 13XP0305A (AdamBatt) and 13XP0258B (Meet Hi-EnD III) are also appreciated. Many thanks to, Ms. Andrea Hilgers, Ms. Marie Theres Gerhards, Dr. Yoo Jung Sohn and Dr. Doris Sebold for carrying out PSD, DTA/TGA, help and support in XRD analysis and SEM imaging, respectively. Very special gratitude to Dr. Enkhtsetseg Dashjav and Dr. Michael Hartmann for providing polymer electrolyte and doing XPS experiments, respectively. Khushnuda Nur: Experimental work, Data extraction, analysis, plotting and interpretation, Writing the Original draft. Christoph Roitzheim: Support for electrochemical test. Sandra Lobe: Performed Raman measurements. Qianli Ma: Performed conductivity measurements. Martin Finsterbusch: Provided LATP powder and lab facilities. Martin Bram: Supervised and guided the work. Olivier Guillon: Supervised and guided the work. The authors report no declarations of interest.

ORCID

Khushnuda Nur https://orcid.org/0000-0001-5460-641X
Qianli Ma https://orcid.org/0000-0002-4709-4927

References

1. Y. Liu, Q. Sun, D. Wang, K. Adair, J. Liang, and X. Sun, *J. Power Sources*, **393**, 193 (2018).
2. C. Sun, J. Liu, Y. Gong, D. P. Wilkinson, and J. Zhang, *Nano Energy*, **33**, 363 (2017).
3. J. Xie, N. Imanishi, T. Zhang, A. Hirano, Y. Takeda, and O. Yamamoto, *J. Power Sources*, **189**, 365 (2009).
4. H. Morimoto, H. Awano, J. Terashima, Y. Shindo, S. Nakanishi, N. Ito, K. Ishikawa, and S. Tobishima, *J. Power Sources*, **240**, 636 (2013).
5. S. Ohta, S. Komagata, J. Seki, T. Saeki, S. Morishita, and T. Asaoka, *J. Power Sources*, **238**, 53 (2013).
6. K. Park, B. C. Yu, J. W. Jung, Y. Li, W. Zhou, H. Gao, S. Son, and J. B. Goodenough, *Chem. Mater.*, **28**, 8051 (2016).
7. L. Miara, A. Windmüller, C. L. Tsai, W. D. Richards, Q. Ma, S. Uhlenbruck, O. Guillon, and G. Ceder, *ACS Appl. Mater. Interfaces*, **8**, 26842 (2016).
8. O. Guillon, J. G. Julian, B. Dargatz, T. Kessel, G. Schiering, and J. Räthel, *Adv. Eng. Mater.*, **16**, 830 (2014).
9. C. E. J. Dancer, *Mater. Res. Express*, **3**, 1 (2016).
10. R. F. Guo, H. R. Mao, Z. T. Zhao, and P. Shen, *Scr. Mater.*, **193**, 103 (2021).
11. J. Guo, H. Guo, A. L. Baker, M. T. Lanagan, E. R. Kupp, G. L. Messing, and C. A. Rangall, *Angew. Chemie - Int. Ed.*, **55**, 11457 (2016).
12. H. Guo, A. Baker, J. Guo, and C. A. Randall, *ACS Nano*, **10**, 10606 (2016).
13. M. Biesuz, G. Taveri, A. I. Duff, E. Olevsky, D. Zhu, C. Hu, and G. Grasso, *Adv. Appl. Ceram.*, **119**, 75 (2020).

14. J. H. Seo, J. Guo, H. Guo, K. Verlinde, D. S. B. Heidary, R. Rajagopalan, and C. A. Randall, *Ceram. Int.*, **43**, 15370 (2017).
15. J. G. P. Sa Silva, M. Bram, A. M. Laptev, J. G. Julian, Q. Ma, F. Tietz, and O. Guillon, *J. Eur. Ceram. Soc.*, **39**, 2697 (2019).
16. H. Leng, J. Huang, J. Nie, and J. Luo, *J. Power Sources*, **391**, 170 (2018).
17. Z. M. Grady, K. Tsuji, A. Ndayishimiye, J. Hwan-Seo, and C. A. Randall, *ACS Appl. Energy Mater.*, **3**, 4356 (2020).
18. K. Nur, C. Roitzheim, M. Finsterbusch, M. Bram, and O. Guillon, *J. Electrochem. Soc.*, **169**, 020556 (2022).
19. Q. Ma, Q. Xu, C. L. Tsai, F. Tietz, and O. Guillon, *J. Am. Ceram. Soc.*, **414**, 410 (2016).
20. Y. Liu et al., *ACS Appl. Mater. Interfaces*, **11**, 27890 (2019).
21. W. Lee, C. K. Lyon, J. H. Seo, R. L. Hallman, Y. Leng, C. Y. Wang, and M. A. Hickner, *C. A. Randall*, **1807872**, 1 (2019).
22. J. H. Seo, Z. Fan, H. Nakaya, R. Rajagopalan, E. D. Gomez, M. Iwasaki, and C. A. Randall, *Jpn. J. Appl. Phys.*, **60**, 037001 (2021).
23. K. Nur, T. P. Mishra, J. G. P. da Silva, J. G. Julian, and M. Bram, *J. Eur. Ceram. Soc.*, **41**, 2648 (2021).
24. J. C. Hunter, *J. Solid State Chem.*, **39**, 142 (1981).
25. W. B. Haines, *J. Agric. Sci.*, **15**, 529 (1925).
26. P. Pierrat and H. S. Caram, *Powder Technol.*, **91**, 83 (1997).
27. M. M. Kohonen, D. Geromichalos, M. Scheel, C. Schier, and S. Herminghaus, *Phys. A Stat. Mech. its Appl.*, **339**, 7 (2004).
28. M. N. Rahaman, *Ceramic Processing and Sintering* (Marcel Dekker Inc, New York) 2nd ed. (2003).
29. B. B. Dargatz, J. G. Julian, M. Bram, Y. Shinoda, F. Wakai, and O. Guillon, *J. Eur. Ceram. Soc.*, **36**, 1221 (2016).
30. B. Key, D. J. Schroeder, B. J. Ingram, and J. T. Vaughey, *Chem. Mater.*, **24**, 287 (2012).
31. R. DeWees and H. Wang, *ChemSusChem*, **12**, 3713 (2019).
32. S. Wang, Y. Ding, G. Zhou, G. Yu, and A. Manthiram, *ACS Energy Lett.*, **1**, 1080 (2016).
33. Z. Ding, J. Li, J. Li, and C. An, *J. Electrochem. Soc.*, **167**, 070541 (2020).
34. Y. Kim, M. Watanabe, A. Takagaki, J. Matsuda, and T. Ishihara, *ChemCatChem*, **11**, 6270 (2019).
35. L. li, Z. Zhang, L. Luo, R. You, J. Jiao, W. Huang, J. Wang, C. Li, X. Han, and S. Chen, *Ionics*, **7**, 3815 (2020).
36. M. Monchak, T. Hupfer, A. Senyshyn, H. Boysen, D. Chernyshow, T. Hansen, K. G. Schell, E. C. Bucharsky, M. J. Hoffmann, and H. Ehrenberg, *Inorg. Chem.*, **55**, 2941 (2016).
37. K. Waetzig, A. Rost, C. Heubner, H. Coeler, K. Nikolowski, M. Wolter, and J. Schilm, *J. Alloys Compd.*, **818**, 153237 (2020).
38. K. Waetzig, A. Rost, U. Langklotz, B. Matthey, and J. Schilm, *J. Eur. Ceram. Soc.*, **36**, 1995 (2016).
39. R. Kali and A. Mukhopadhyay, *J. Power Sources*, **247**, 920 (2014).
40. D. Rettenwander, A. Welzl, S. Pristat, F. Tietz, S. Taibl, G. J. Redhammer, and J. Fleig, *J. Mater. Chem. A*, **4**, 1506 (2015).
41. M. Vinnichenko, K. Waetzig, A. Aurich, C. Baumgartner, M. Hermann, C. W. Ho, M. Kusnezoff, and C. W. Lee, *Nanomaterials*, **12**, 3178 (2022).
42. K. Waetzig, C. Heubner, and M. Kusnezoff, *Crystals*, **10**, (5)408 (2020).
43. P. Tarte, A. Rulmont, and C. Merckaert-Ansay, *Spectrochim. Acta*, **42**, 1009 (1986).
44. B. E. Francisco, C. R. Stoldt, and J. C. M'Peko, *J. Phys. Chem. C*, **119**, 16432 (2015).
45. S. Ghosh, C. Sudarshan, and C. Sudakar, *J. Appl. Phys.*, **133**, 0 (2023).
46. E. Dashjav, Q. Ma, Q. Xu, C. L. Tsai, M. Giarola, G. Mariotto, and F. Tietz, *J.ssi.*, **321**, 83 (2018).
47. M. Giarola, A. Sanson, F. Tietz, S. Pristat, E. Dashjav, D. Rettenwander, G. J. Redhammer, and G. Mariotto, *J. Phys. Chem. C*, **121**, 3697 (2017).
48. S. Soman, Y. Iwai, J. Kawamura, and A. Kulkarni, "Crystalline phase content and ionic conductivity correlation in LATP glass-ceramic." *J. Solid State Electrochem.*, **16**, 1761 (2012).
49. S. Mandal, J. M. Amarilla, J. Ibáñez, and J. M. Rojo, *J. Electrochem. Soc.*, **148**, 24 (2001).
50. A. Kay, *United States Pat. (10) Pat.*, No.US 8,784,694 B2**2** (2014).